THE JOURNAL OF PHYSICAL CHEMISTRY C
A JOURNAL OF THE AMERICAN CHEMICAL SOCIETY

pubs.acs.org/JPCC

Article

Vibrational Properties of a Naturally Occurring Semiconducting van der Waals Heterostructure

Viviane Zurdo Costa, Liangbo Liang, Sam Vaziri, Addison Miller, Eric Pop, and A. K. M. Newaz*

Cite This: *J. Phys. Chem. C* 2021, 125, 21607−21613

Read Online

ACCESS | Metrics & More | Article Recommendations | Supporting Information

ABSTRACT: We present vibrational properties of Franckeite, which is a naturally occurring van der Waals heterostructure consisting of two different semiconducting layers. Franckeite is a complex layered crystal composed of alternating SnS_2-like pseudohexagonal and PbS-like pseudotetragonal layers stacked on top of each other, providing a unique platform to study vibrational properties and thermal transport across layers with mass density and phonon mismatches. Using micro-Raman spectroscopy and first-principles Raman simulations, we found that the PbS-like pseudotetragonal structure is mostly composed of Pb_3SbS_4. We also discovered several low-frequency Raman modes that originate from the intralayer vibrations of the pseudotetragonal layer. Using density functional theory, we determined all vibrational patterns of Franckeite, whose signatures are observed in the Raman spectrum. By studying temperature-dependent Raman spectroscopy (300−500 K), we have found different temperature coefficients for both pseudotetragonal and pseudohexagonal layers. We believe that our study will help understand the vibration modes of its complex heterostructure and the thermal properties at the nanoscale.

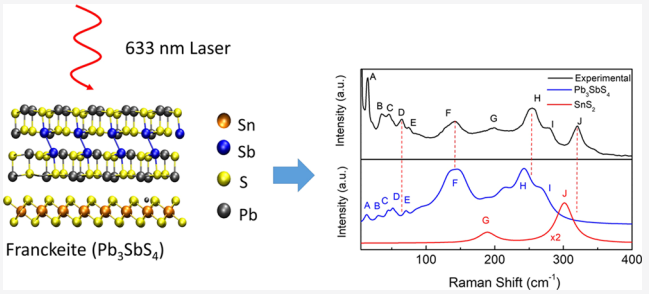

INTRODUCTION

Van der Waals (vdW) heterostructures obtained by stacking dissimilar two-dimensional (2D) materials such as graphene (Gr), transition-metal dichalcogenides (TMDs), or hexagonal boron nitride (*h*BN) have become a major research direction in condensed matter physics owing to novel electronic states and applications that may be realized in these vertical heterostructures.[1−6] These designer vdW heterostructures can demonstrate electronic, optical, and thermal properties that strongly differ from those of the constituent 2D materials, thus opening the door to obtain on-demand interesting physical, electrical, optical, optoelectrical behavior, and thermal properties, such as moiré exciton,[7,8] and strongly correlated quantum phenomena, including tunable Mott insulators at half-filling,[9,10] unconventional superconductivity near integer filling,[11−13] and ferromagnetism.[14] The standard fabrication method of all of these heterostructures includes manual or robotic vertical assembly of 2D stacks using deterministic placement methods.[5,15,16] Because of manual stacking, the neighboring layer interface may contain fabrication artifacts, such as foreign particles or bubbles between the interfaces, which may affect the measurement of intrinsic physical properties.[17−20] Hence, it is critical to measure intrinsic physical properties of interfaces with van der Waals heterostructures free of fabrication artifacts. We present here vibrational properties of a naturally grown van der Waals superlattices layered semiconductor, Franckeite, which is free from fabrication artifacts between semiconducting layers.[17−21]

Franckeite is a heterostructure composed of alternating sequences of weakly bound stacked PbS-like pseudotetragonal (Q) layers and SnS_2-like pseudohexagonal (H) layers attached by van der Waals interactions.[17−19] Thus, Franckeite (Fr) can be considered a naturally occurring vdW heterostructure analogue of its lab-fabricated other 2D vdWHs. Recently, several groups have demonstrated exfoliation of Franckeite (mechanically and by liquid-phase exfoliation) down to the single unit cell, and exfoliated flakes have been assembled into electronic devices, energy conversion devices, and photodetectors operating in the near-infrared range.[17−19,21]

Though Fr provides a fascinating 2D crystal heterostructure with possibilities of exploring new physics and developing many attractive applications, some of its fundamental properties remain unknown. First, though the crystal structure of the H-layer is known (SnS_2), the composition crystal structure of the Q-layer is highly debated. It is also unclear whether pseudotetragonal (Q) layer is predominantly made of Pb_3SbS_4 or it is Sn-based $PbSnS_2$. Second, the Raman spectroscopy of Fr is not understood. Because Fr contains two different layered semiconducting materials, it may provide unique vibrational

Received: June 14, 2021
Revised: September 7, 2021
Published: September 23, 2021

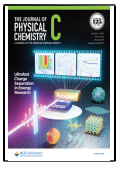

https://doi.org/10.1021/acs.jpcc.1c05241
J. Phys. Chem. C 2021, 125, 21607−21613

behavior because of mass density and phonon mismatches. Here, we answer these fundamental questions by performing micro-Raman spectroscopy and first-principles density functional theory (DFT) studies. First, we determine the composition of the crystal structure of the pseudotetragonal Q-layer. Second, we conduct extensive Raman spectroscopy of Fr and discover several low-frequency Raman modes starting at 15 cm^{-1}. Third, we identify the vibrational modes responsible for the Raman-active behavior using DFT calculations. Fourth, we perform the temperature-dependent Raman spectroscopy of Fr vdW heterostructure for the first time to identify the thermal behavior of different semiconducting layers.

We present our experimental and computational study of Raman spectroscopy of thermodynamically stable Franckeite-immobilized flakes on the SiO_2 (90 nm)/p^+Si substrate. The bulk Fr crystals were obtained from San Jose mine in Bolivia. We have prepared the sample using microexfoliation from bulk samples. We have confirmed the thermodynamic stability by investigating few-layer Fr flakes by optically imaging the sample. We have observed no difference in the image of few-layer Fr even after 18 months stored in an ambient condition (see the Supporting Information). Since we prepared the microexfoliated sample reported here and the sample reported in an earlier publication from the same bulk crystal, we point the reader to the work by Ray et al., for a detailed characterization of Franckeite by energy-dispersive X-ray (EDX) and a scanning electron microscope.[19] Also, detailed characterizations and high-resolution transmission electron microscope images of Fr are reported in the pioneering work by Velický et al.,[18] and Molina-Mendoza et al.[17]

MATERIALS AND METHODS

Sample Fabrication. Fr samples immobilized on different substrates were prepared by microexfoliation using polyimide tape of 0.015 mm of thickness and an adhesive layer of 0.06 mm of thickness, followed by characterization using optical microscopy. Raman spectroscopy and atomic force microscopy (AFM) were performed to verify the franckeite deposition and determine the sample thickness. The suspended Fr samples were picked up and dropped off via the dry-transfer technique with poly(ethylene terephthalate) (PET) stamp on TEM 2000 (aperture size ~7.5 μm) mesh grids attached to a 90 nm SiO_2 substrate with a double-sided Kapton tape.

Raman Characterization. Confocal micro-Raman measurements were performed using a commercial equipment (Horiba LabRAM Evolution). A long working-distance 100× objective lens with a numerical aperture of 0.6 was used. The excitation source was a 633 nm laser of power ~200 μW. The Raman spectra were measured using a grating with 600 g/mm blazed at 500 nm and a solid-state-cooled CCD detector. To measure the temperature-dependent Raman, we calibrated the temperature of the sample with a Linkam THMS600 stage in ambient air using the Si Raman peak.

DFT Calculations. We performed first-principles density functional theory (DFT) calculations using the plane-wave VASP package, where projector augmented wave (PAW) pseudopotentials were used for electron−ion interactions[22] and the Perdew−Burke−Ernzerhof (PBE) functional was for exchange−correlation interactions.[23,24] Van der Waals (vdW) interactions were included using the DFT-D3 method. Individual Pb_3SbS_4, $PbSnS_2$, and SnS_2 layers were modeled for phonon and Raman scattering calculations, where Pb_3SbS_4 or $PbSnS_2$ is commonly considered as the structure of the Q-layer in Franckeite, while SnS_2 is considered as the H-layer in Franckeite.[17−19] Note that Franckeite, a naturally occurring vdW heterostructure, exhibits a noncommensurate layer match between the Q and H layers, and thus it would be computationally too costly for direct phonon and Raman calculations of the whole Franckeite heterostructure. Because interactions between the layers are weak, the phonon and Raman features of the Franckeite heterostructure can be described by its individual component layers, i.e., Pb_3SbS_4 (or $PbSnS_2$) and SnS_2. Single-layer Pb_3SbS_4, $PbSnS_2$, and SnS_2 were modeled by a periodic slab geometry, where a vacuum separation of at least 21 Å in the out-of-plane direction (i.e., z-direction) was set to avoid spurious interactions between periodic images. For 2D slab calculations, a 12 × 12 × 1 k-point sampling was used for Pb_3SbS_4 and $PbSnS_2$, while a 24 × 24 × 1 k-point sampling was for SnS_2. For all systems, the cutoff energy was chosen as 350 eV, and all atoms were relaxed until the residual forces were below 0.001 eV/Å. Note that in-plane lattice constants were optimized using the method of fixing the total volume (ISIF = 4 in VASP) to avoid the collapse of the vacuum separation in the z-direction.

Based on fully relaxed structures, phonon calculations were carried out using the finite difference scheme implemented in the Phonopy software to obtain phonon frequencies and eigenvectors.[25] Hellmann−Feynman forces in the supercell (2 × 2 × 1 for Pb_3SbS_4 and $PbSnS_2$, while 3 × 3 × 1 for SnS_2) were computed by VASP for both positive and negative atomic displacements (δ = 0.03 Å) and then used in Phonopy to construct the dynamic matrix, whose diagonalization provides phonon frequencies and phonon eigenvectors (i.e., vibrations). Raman scattering calculations were then performed within the Placzek approximation using the in-house developed Raman modeling package.[26−28] For the jth phonon mode, Raman intensity is $I \propto \frac{(n_j+1)}{\omega_j}|e_i\cdot\tilde{R}\cdot e_s^T|^2$, where e_i and e_s are the electric polarization vectors of the incident and scattered light, respectively, and $\tilde{R}$ is the Raman tensor of the phonon mode.[29] ω_j is the frequency of the jth phonon mode and $n_j = (e^{\hbar\omega_j/k_BT}-1)^{-1}$ is its Boltzmann distribution function at the given temperature T = 300 K. The matrix element of the (3 × 3) Raman tensor $\tilde{R}$ of the jth phonon mode is[26,27,29]

$$\tilde{R}_{\alpha\beta}(j) = V_0 \sum_{\mu=1}^{N}\sum_{l=1}^{3} \frac{\partial\chi_{\alpha\beta}}{\partial r_l(\mu)} \frac{e_l^j(\mu)}{\sqrt{M_\mu}}$$

where $\chi_{\alpha\beta} = (\varepsilon_{\alpha\beta}-\delta_{\alpha\beta})/4\pi$ is the electric polarizability tensor related to the dielectric tensor $\varepsilon_{\alpha\beta}$, $r_l(\mu)$ is the position of the μth atom along the direction, l, $\frac{\partial\chi_{\alpha\beta}}{\partial r_l(\mu)}$ is the derivative of the polarizability tensor (essentially the dielectric tensor) over the atomic displacement, $e_l^j(\mu)$ corresponds to the displacement of the μth atom along the direction l in the jth phonon mode (i.e., the eigenvector of the dynamic matrix), M_μ is the mass of the μth atom, and V_0 is the unit cell volume. For both positive and negative atomic displacements (δ = 0.03 Å) in the unit cell, dielectric tensors $\varepsilon_{\alpha\beta}$ were computed by VASP[30] and then their derivatives were obtained via the finite difference scheme. Based on phonon frequencies, phonon eigenvectors, and the derivatives of dielectric tensors, Raman tensor $\tilde{R}$ of any phonon mode can be obtained, which subsequently yields the Raman intensity $I(j)$ under a given laser polarization setup. In the typical back-scattering laser geometry (i.e., the light travels in and out along the z-direction), the electric polarization vectors

https://doi.org/10.1021/acs.jpcc.1c05241
J. Phys. Chem. C 2021, 125, 21607−21613

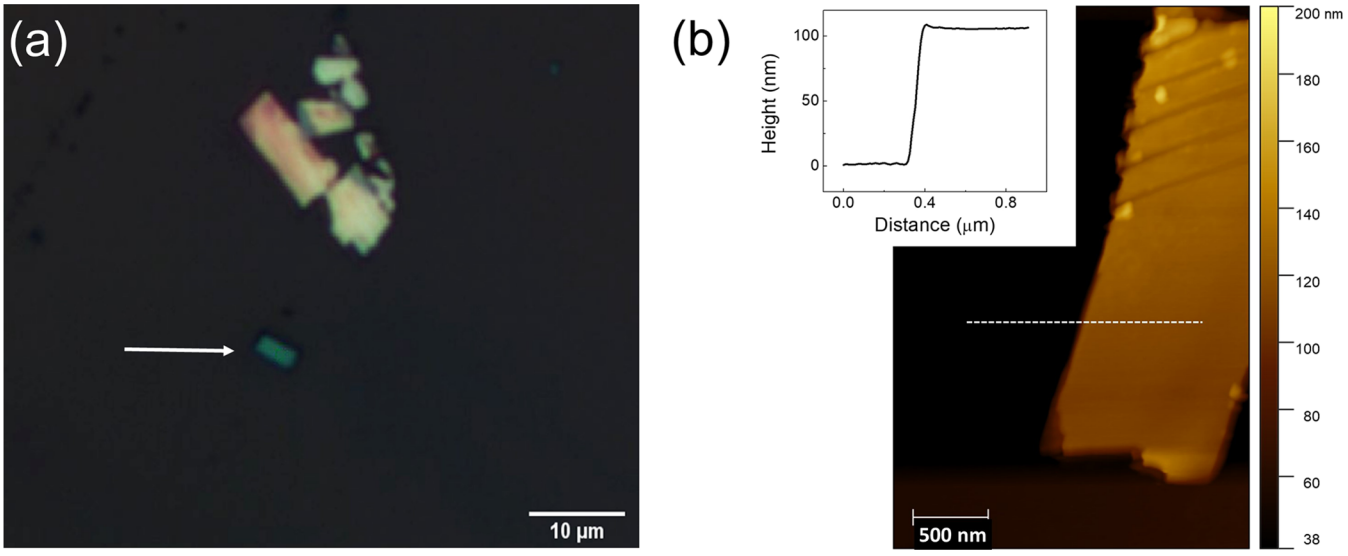

Figure 1. Optical and atomic force microscope images of a Franckeite sample. (a) Optical image of the sample used in the study (marked by an arrow). The sample is immobilized on a SiO_2 (90 nm)/p^+Si substrate. (b) AFM image of the same sample is shown in (a). The sample thickness is ~100 nm. The inset is showing the height profile along the dashed line mark in the main panel.

of incoming and scattered light (e_i and e_s) are in the $x-y$ plane. Averaging over all possible in-plane polarizations, the Raman intensity of any given mode in the experimental unpolarized laser configuration is given by

$$I \propto \frac{1}{4}\frac{(n_j+1)}{\omega_j}(|\tilde{R}_{11}|^2 + |\tilde{R}_{12}|^2 + |\tilde{R}_{21}|^2 + |\tilde{R}_{22}|^2)$$

Finally, based on the calculated Raman intensities $I(j)$ and phonon frequencies ω_j, the Raman spectrum can be obtained after Lorentzian broadening.

RESULTS AND DISCUSSION

Figure 1 shows the optical and atomic force microscope (AFM) images of the microexfoliated sample. The flake SiO_2/p^+Si substrate studied in this experiment is marked by an arrow, as shown in Figure 1a. Figure 1b shows the AFM image of the sample. The sample thickness is ~100 nm as seen in the height profile presented in the inset of Figure 1b.

Figure 2a top panel presents the Raman spectrum of Fr measured at room temperature. We have observed many Raman modes, as A(15 cm^{-1}), B(35 cm^{-1}), C(45 cm^{-1}), D(64 cm^{-1}), E(75 cm^{-1}), F(140 cm^{-1}), G(195 cm^{-1}), H(256 cm^{-1}), I(276 cm^{-1}), and J(321 cm^{-1}). The peak positions of well-defined peaks, A, H, and J peaks, were determined using Gaussian fitting (see the Supporting Information for the Gaussian fitting of room temperature Raman spectra. The other peak values were determined roughly from the maximum Raman intensity counts).

We used a commercially available micro-Raman setup (Horiba LabRAM Evolution). We studied micro-Raman spectroscopy using both 532 and 633 nm excitation lasers and we observed that the Raman intensity is much larger with 633 nm laser than that by 532 nm laser (Figure S2 in the Supporting Information). Differential reflectivity measurements confirmed higher absorption in the red range, suggesting resonance-enhanced Raman modes with a 633 nm excitation source (see Figure S3 in the Supporting Information). In the rest of the study, we present our results with the 633 nm laser, which has a beam width ~1 μm. We have observed 10 clearly

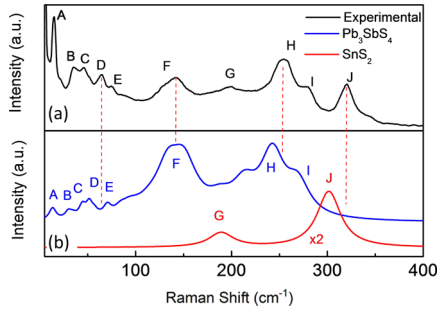

Figure 2. Raman spectroscopy of many-layer Franckeite. (a) Experimentally measured Raman spectroscopy at room temperature. The excitation laser wavelength is 633 nm. The Raman modes are marked alphabetically as A(15 cm^{-1}), B(35 cm^{-1}), C(45 cm^{-1}), D(64 cm^{-1}), E(75 cm^{-1}), F(140 cm^{-1}), G(195 cm^{-1}), H(256 cm^{-1}), I(276 cm^{-1}), and J(321 cm^{-1}). (b) Calculated Raman spectra of Franckeite are shown here. The blue line presents the Raman modes for Pb_3SbS_4 and the red line for SnS_2.

distinguishable peaks from the low-frequency regime, as low as to 15 cm^{-1}, to the high-frequency regime. The low-frequency Raman modes are important to understand the crystal structure as well as the interlayer coupling.[31] To the best of our knowledge, we are reporting the low-frequency Raman of Franckeite for the first time.

The Raman peaks near 140, 195, 256, 276, and 321 cm^{-1} were reported by Velický et al. and us.[18,19] It has been argued previously that two peaks at 256 and 276 cm^{-1} originate from stibnite (Sb_2S_3) and the peak at 321 cm^{-1} is from berndtite (SnS_2) in the H-layer, respectively. The peaks at 43 and 199 cm^{-1} may originate from the PbS lattices and SnS_2 lattices.[17−19] The origin of different Raman peaks, particularly the low-frequency Raman modes we discovered, are still not completely understood, and their atomic vibrational patterns are not yet revealed. Hence, a detailed study is necessary to elucidate the origin of different Raman peaks in Fr.

To determine the crystal structure of Franckeite by Raman spectroscopy, we performed first-principles DFT calculations using the plane-wave VASP package.[22−24] Individual Pb_3SbS_4,

https://doi.org/10.1021/acs.jpcc.1c05241
J. Phys. Chem. C 2021, 125, 21607−21613

$PbSnS_2$, and SnS_2 layers were modeled for phonon and Raman scattering calculations, where Pb_3SbS_4 or $PbSnS_2$ is commonly considered as the structure of a Q-layer, while SnS_2 is considered as an H-layer in Franckeite (see the Materials and Methods section for details).[17−19] We note that Q and H layers are incommensurate in Franckeite, and therefore it is computationally prohibitive for direct phonon and Raman calculations of the whole heterostructure. Since interactions between the layers are weak, the Raman features of the heterostructure should be close to the composition of individual layers.

According to our calculations, the Pb_3SbS_4 layer has no symmetry (its crystal structure is shown in Figure 3 as part of Franckeite), so every phonon mode is Raman active in principle, which could explain why many Raman peaks are appearing in the experimental Raman spectra. This makes the phonon/Raman analysis challenging. By computing Raman intensities of Pb_3SbS_4, we can determine phonon modes with strong Raman signals to compare with the experimentally measured Raman peaks. The SnS_2 layer, however, has high symmetry and it only has two distinctive Raman modes: one at 189 cm^{-1} with E_g symmetry, and the other one at 302 cm^{-1} with A_{1g} symmetry.

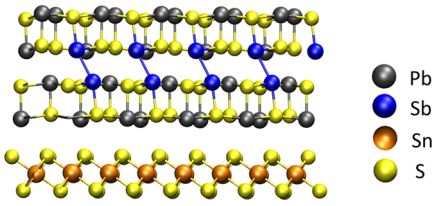

Figure 3. Crystal structure of Franckeite used for calculating the Raman spectra. The top is the Q-layer (Pb_3SbS_4) and the bottom is the H-layer (SnS_2). The colors assigned to different atoms are shown on the right.

We have found that the experimentally measured Raman peaks are in good agreement with the calculated ones from Pb_3SbS_4 and SnS_2 layers (see Figure 2 for comparison). The experimentally measured and first-principles calculated Raman peaks are also listed in Table 1. We also computed Raman peaks of $PbSnS_2$ and SnS_2 layers for comparison with the experimental data of Franckeite (Figure S1 in the Supporting Information), where the mismatch can be clearly seen. For example, in the experimental Raman spectra, a peak I (276 cm^{-1}) appears as a right shoulder peak of peak H (256 cm^{-1}); however, the $PbSnS_2$ layer does not exhibit such a distinctive feature and instead shows only one distinguishable peak around 271 cm^{-1} (Figure S1 in the Supporting Information), according to our calculations. In contrast, the computed Raman profile of the Pb_3SbS_4 layer reproduces the experimentally observed shoulder peak feature (Figure 2). These results suggest that the Q-layer is mostly like composed of Pb_3SbS_4 instead of $PbSnS_2$. Furthermore, in the low-frequency region, our calculations also show that Raman peaks of the Pb_3SbS_4 layer match better with experimental ones than those of the $PbSnS_2$ layer. With the crystal structure of the Q-layer in Franckeite determined, we then computed the atomic vibrational patterns of all Raman peaks, including the low-frequency and high-frequency ones, and illustrate them in Figure 4.

Table 1. Different Raman Modes Measured Experimentally and Determined Using First-Principles Calculations

low-frequency modes calculations (cm^{-1})	experiment (cm^{-1})	high-frequency modes calculations (cm^{-1})	experiment (cm^{-1})
13	15	145	140
30	35	189	195
45	45	243	256
51	64	269	276
71	75	302	321

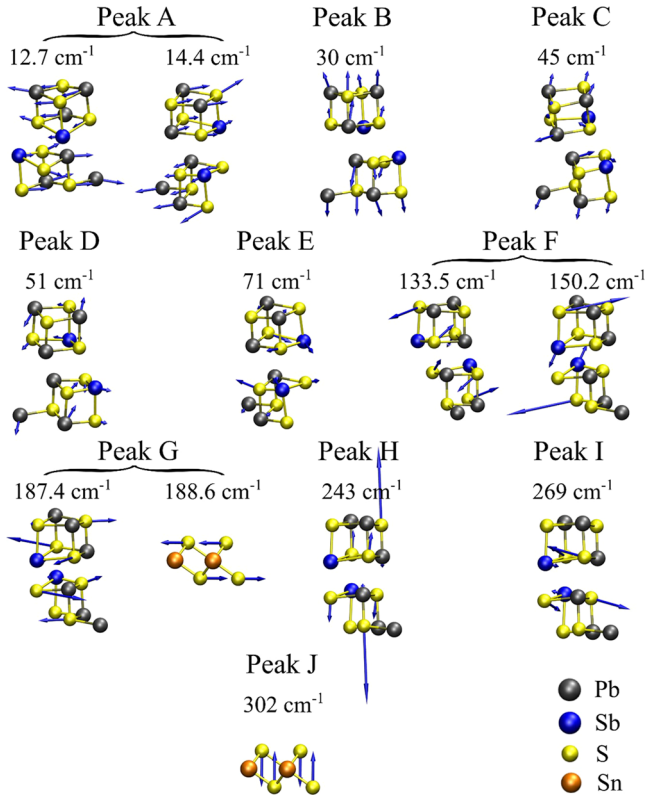

Figure 4. Calculated atomic vibrational patterns of experimental Raman peaks A−J in Franckeite. Raman modes from the Q-layer (Pb_3SbS_4) and the H-layer (SnS_2) are shown separately. The calculated phonon frequencies are shown for each mode. The symbols for different atoms are shown in the bottom right. Since the Pb_3SbS_4 layer has no symmetry, every phonon mode is Raman active in principle, and thus there are many Raman peaks showing up in the experimental Raman spectra. Furthermore, some Raman peaks are contributed by multiple phonon modes close to each other (e.g., peak A, peak F, peak G, etc.), which contribute to the large widths of Raman peaks in the experimental data. The SnS_2 layer has high symmetry, and it only has two distinctive Raman modes: one around 188.6 cm^{-1} (contributing to peak G), and the other one around 302 cm^{-1} (corresponding to peak J). Other Raman peaks primarily originate from vibrations of the Pb_3SbS_4 layer.

Finally, we acknowledge that there is still a discrepancy between the calculated and experimental Raman frequencies and intensities shown in Figure 2 and Table 1. It is common that DFT calculations underestimate phonon frequencies due to approximations adopted in the DFT methodology. The computed Raman intensities are not in exactly quantitative match with experimental ones owing to the adopted Placzek approximation and other factors missing in the calculations, such as substrate effects, resonant Raman effects, etc. In

https://doi.org/10.1021/acs.jpcc.1c05241
J. Phys. Chem. C 2021, 125, 21607−21613

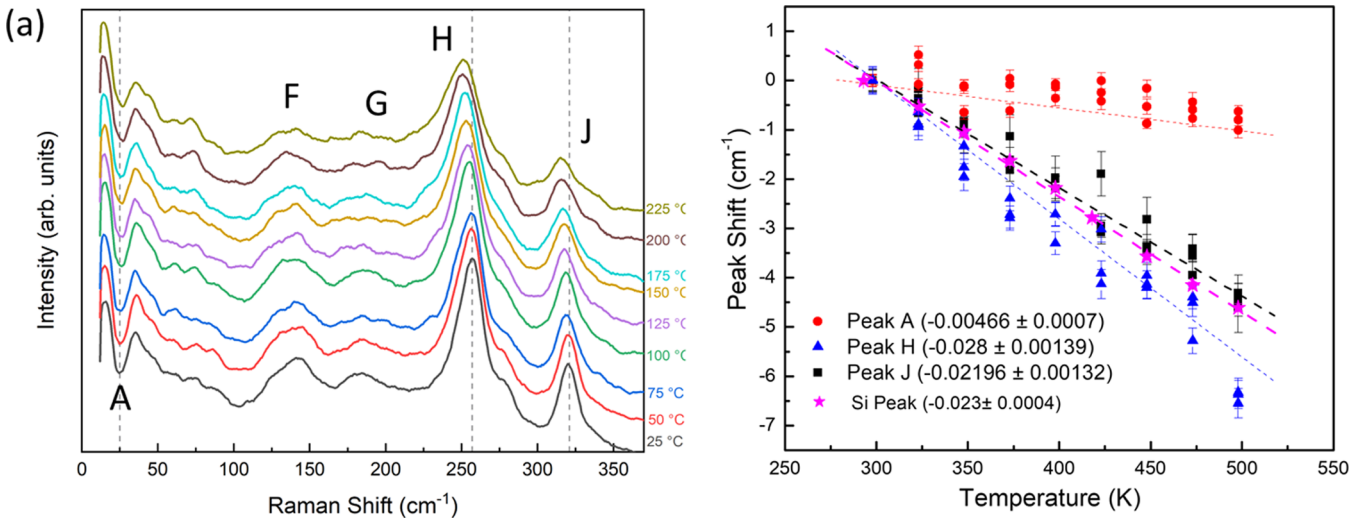

Figure 5. Temperature dependence of different vibrational modes. (a) Raman spectra at different temperatures from 25 to 225 °C. All peaks are shifting to lower Raman shift values as we increase the temperature. (b) Peak shift positions ($\Delta = \omega_{RT} - \omega_T$, where ω_{RT} and ω_T are peak positions at room temperature and temperature T, respectively) of three representative Raman peaks: low-frequency mode A (red circle), Pb_3SbS_4 peak H (blue triangle), and SnS_2 peak J (black square). The temperature variation of the Si substrate Raman peak is also shown (magenta star). We clearly see that all four peaks are evolving at different rates with respect to temperature. The temperature coefficients of all four peaks are shown next to the legends.

addition, individual Q and H monolayers are modeled in our DFT calculations instead of the realistic large vdW heterostructure with many layers due to the computational cost. Furthermore, the experimental structure contains substitutions of other elements such as Fe. Modeling of the exact experimental structure is very challenging since it requires a large supercell incorporating a small concentration of substitutional elements. Nevertheless, our calculated Raman spectra capture most of the experimental Raman features as seen in Figure 2 and Table 1, such as numerous low-frequency Raman peaks, the distinctive shoulder peak feature formed between peak H and peak J, the broad peak F, the weak peak G, and the highest-frequency peak J from the SnS_2 layer.

To understand the effect of the Fr thickness on Raman modes, we performed room temperature Raman measurement of samples with a wide range of thickness from 6 to 100 nm. We have observed two important characteristics. First, we observed that Raman peaks are independent of a wide range of Fr thickness from ∼6 to ∼100 nm (Figure S4 in the Supporting Information). Second, we have not detected any Raman signal for samples below 6 nm.

Now, we shift our focus to temperature-dependent Raman spectroscopy. We have conducted Raman spectroscopy over a wide range of temperatures ranging from 294 K (room temperature) to 500 K. The Raman spectra at different temperature are shown in Figure 5a, revealing a redshift of the Raman peak as we increase the temperature. We observed that different Raman peaks shift at different rates.

Because the measured Raman peaks are broad, we determined the Raman peak position and errors using Gaussian fitting.[32] To enhance visualization of the temperature-dependent Raman shift, we have calculated the peak shift, $\Delta = \omega_{RT} - \omega_T$, where ω_{RT} and ω_T are peak positions at room temperature (∼294 K) and temperature T, respectively. The peak shift, Δ, of low-frequency mode A peak, Pb_3SbS_4 peak H, and SnS_2 peak J are presented in Figure 5b. We observed a higher rate of redshift for H and J peaks compared to the low-frequency A mode. To quantify the Raman shift as a function of temperature, we have used least-squares fitting to determine the slope as $\omega = \omega_0 + \alpha T$. Here, α is the first-order temperature coefficient and ω_0 is the Raman peak at the zero temperature.

We have measured the temperature coefficient $\alpha = 4.66 \times 10^{-3}$, 28×10^{-3}, and 22×10^{-3} cm^{-1}/K for A, H, and J peaks, respectively. We have found that the temperature coefficient of the substrate Si is 23×10^{-3} cm^{-1}/K (see the Supporting Information for Si Raman spectrums at different temperatures). Intriguingly, we note that the temperature coefficient for the low-frequency peak is an order of magnitude lower than high-frequency modes. Comparing to the reported values of other 2D-layered materials, the temperature coefficients reported for the G peak in graphene, A_{1g} mode in monolayer WS_2, and A_{1g} in monolayer MoS_2 are 16×10^{-3}, 12×10^{-3}, and 15×10^{-3} cm^{-1}/K, respectively.[33−35] The temperature coefficients of both H and J peaks in Fr are larger than the temperature coefficients of Raman peaks in graphene and MoS_2. The behavior of the rate of change in the Raman peak position with temperature can vary for different phonon modes as well as for different materials.[36] The variation of the first-order temperature coefficient of the Raman peak position of the normal modes is mainly due to the contribution from thermal expansion or volume contribution and from the temperature contribution that results from anharmonicity.[36]

We have observed that the full width at half-maximum (FWHM) increases significantly for both F and G peaks as shown in Figure 5a, whereas there is a negligible FWHM increment for the low-frequency mode as we increase the temperature. The peak height also decreases for all three peaks as the temperature increases (Figure S5 in the Supporting Information).

In conclusion, we have determined the composition of the crystal structure and vibrational properties of Fr using Raman spectroscopy and first-principles Raman simulations. We have demonstrated the vibrational properties of Fr and how those phonon vibrations depend on temperatures by measuring the temperature-dependent Raman modes. Our study will help

https://doi.org/10.1021/acs.jpcc.1c05241
J. Phys. Chem. C 2021, 125, 21607−21613

understand the atomic structure and vibrational modes of a natural heterostructure and its heat transport management at the nanoscale.

■ ASSOCIATED CONTENT

Supporting Information

The Supporting Information is available free of charge at https://pubs.acs.org/doi/10.1021/acs.jpcc.1c05241.

Raman calculation of $PbSnS_2$, Raman data for 632 and 532 nm laser excitation, differential reflectivity measurement data, Raman spectra for different thickness of Franckeite, temperature-dependent Raman spectroscopy of Franckeite, temperature-dependent Raman spectroscopy of silicon, Gaussian fitting of the Raman peak, and thermal stability of the sample (PDF)

■ AUTHOR INFORMATION

Corresponding Author

A. K. M. Newaz − *Department of Physics and Astronomy, San Francisco State University, San Francisco, California 94132, United States;* orcid.org/0000-0001-8159-1604; Phone: 415-338-2944; Email: akmnewaz@sfsu.edu

Authors

Viviane Zurdo Costa − *Department of Physics and Astronomy, San Francisco State University, San Francisco, California 94132, United States*

Liangbo Liang − *Center for Nanophase Materials Sciences, Oak Ridge National Laboratory, Oak Ridge, Tennessee 37831, United States;* orcid.org/0000-0003-1199-0049

Sam Vaziri − *Department of Electrical Engineering, Stanford University, Stanford, California 94305, United States;* orcid.org/0000-0003-1234-6060

Addison Miller − *Department of Physics and Astronomy, San Francisco State University, San Francisco, California 94132, United States*

Eric Pop − *Department of Electrical Engineering, Stanford University, Stanford, California 94305, United States; Department of Materials Science and Engineering and Precourt Institute for Energy, Stanford University, Stanford, California 94305, United States;* orcid.org/0000-0003-0436-8534

Complete contact information is available at: https://pubs.acs.org/10.1021/acs.jpcc.1c05241

Notes

The authors declare no competing financial interest.

■ ACKNOWLEDGMENTS

V.Z.C. and A.K.M.N. acknowledge the support from the Department of Defense Award (ID: 72495RTREP). A.K.M.N. also acknowledges the support from the National Science Foundation Grant ECCS-1708907. All AFM measurements were supported by NSF for instrumentation facilities (NSF MRI-CMMI 1626611). Raman spectroscopy data were acquired at the Stanford Nano Shared Facilities (SNSF) and at SFSU, supported by the National Science Foundation under award ECCS-2026822 and DMR-1828476. A portion of this research (Raman scattering modeling) used resources at the Center for Nanophase Materials Sciences, which is a U.S. Department of Energy Office of Science User Facility. L.L. acknowledges computational resources of the Compute and Data Environment for Science (CADES) at the Oak Ridge National Laboratory, which is supported by the Office of Science of the U.S. Department of Energy under Contract no. DE-AC05-00OR22725.

■ REFERENCES

(1) Geim, A. K.; Grigorieva, I. V. Van der Waals heterostructures. *Nature* **2013**, *499*, 419−425.

(2) Liu, Y.; Weiss, N. O.; Duan, X.; Cheng, H.-C.; Huang, Y.; Duan, X. Van der Waals heterostructures and devices. *Nat. Rev. Mater.* **2016**, *1*, No. 16042.

(3) Novoselov, K. S.; Mishchenko, A.; Carvalho, A.; Castro Neto, A. H. 2D materials and van der Waals heterostructures. *Science* **2016**, *353*, No. aac9439.

(4) Liao, W.; Huang, Y.; Wang, H.; Zhang, H. Van der Waals heterostructures for optoelectronics: Progress and prospects. *Appl. Mater. Today* **2019**, *16*, 435−455.

(5) Frisenda, R.; Navarro-Moratalla, E.; Gant, P.; Perez De Lara, D.; Jarillo-Herrero, P.; Gorbachev, R. V.; Castellanos-Gomez, A. Recent progress in the assembly of nanodevices and van der Waals heterostructures by deterministic placement of 2D materials. *Chem. Soc. Rev.* **2018**, *47*, 53−68.

(6) Novoselov, K. S.; Mishchenko, A.; Carvalho, A.; Castro Neto, A. H. 2D materials and van der Waals heterostructures. *Science* **2016**, *353*, No. aac9439.

(7) Yu, H.; Liu, G.-B.; Tang, J.; Xu, X.; Yao, W. Moiré excitons: From programmable quantum emitter arrays to spin-orbit−coupled artificial lattices. *Sci. Adv.* **2017**, *3*, No. e1701696.

(8) Wu, F.; Lovorn, T.; MacDonald, A. H. Topological Exciton Bands in Moiré Heterojunctions. *Phys. Rev. Lett.* **2017**, *118*, No. 147401.

(9) Cao, Y.; Fatemi, V.; Demir, A.; Fang, S.; Tomarken, S. L.; Luo, J. Y.; Sanchez-Yamagishi, J. D.; Watanabe, K.; Taniguchi, T.; Kaxiras, E.; Ashoori, R. C.; Jarillo-Herrero, P. Correlated insulator behaviour at half-filling in magic-angle graphene superlattices. *Nature* **2018**, *556*, 80.

(10) Chen, G.; Jiang, L.; Wu, S.; Lyu, B.; Li, H.; Chittari, B. L.; Watanabe, K.; Taniguchi, T.; Shi, Z.; Jung, J.; Zhang, Y.; Wang, F. Evidence of a gate-tunable Mott insulator in a trilayer graphene moiré superlattice. *Nat. Phys.* **2019**, *15*, 237−241.

(11) Cao, Y.; Fatemi, V.; Fang, S.; Watanabe, K.; Taniguchi, T.; Kaxiras, E.; Jarillo-Herrero, P. Unconventional superconductivity in magic-angle graphene superlattices. *Nature* **2018**, *556*, 43.

(12) Yankowitz, M.; Chen, S.; Polshyn, H.; Zhang, Y.; Watanabe, K.; Taniguchi, T.; Graf, D.; Young, A. F.; Dean, C. R. Tuning superconductivity in twisted bilayer graphene. *Science* **2019**, *363*, 1059−1064.

(13) Lu, X.; Stepanov, P.; Yang, W.; Xie, M.; Aamir, M. A.; Das, I.; Urgell, C.; Watanabe, K.; Taniguchi, T.; Zhang, G.; Bachtold, A.; MacDonald, A. H.; Efetov, D. K. Superconductors, orbital magnets and correlated states in magic-angle bilayer graphene. *Nature* **2019**, *574*, 653−657.

(14) Sharpe, A. L.; Fox, E. J.; Barnard, A. W.; Finney, J.; Watanabe, K.; Taniguchi, T.; Kastner, M. A.; Goldhaber-Gordon, D. Emergent ferromagnetism near three-quarters filling in twisted bilayer graphene. *Science* **2019**, *365*, 605−608.

(15) Dean, C. R.; Young, A. F.; Meric, I.; Lee, C.; Wang, L.; Sorgenfrei, S.; Watanabe, K.; Taniguchi, T.; Kim, P.; Shepard, K. L.; Hone, J. Boron nitride substrates for high-quality graphene electronics. *Nat. Nanotechnol.* **2010**, *5*, 722−726.

(16) Masubuchi, S.; Morimoto, M.; Morikawa, S.; Onodera, M.; Asakawa, Y.; Watanabe, K.; Taniguchi, T.; Machida, T. Autonomous robotic searching and assembly of two-dimensional crystals to build van der Waals superlattices. *Nat. Commun.* **2018**, *9*, No. 1413.

(17) Molina-Mendoza, A. J.; Giovanelli, E.; Paz, W. S.; Niño, M. A.; Island, J. O.; Evangeli, C.; Aballe, L.; Foerster, M.; van der Zant, H. S. J.; Rubio-Bollinger, G.; Agraït, N.; Palacios, J. J.; Pérez, E. M.;

Castellanos-Gomez, A. Franckeite as a naturally occurring van der Waals heterostructure. *Nat. Commun.* **2017**, *8*, No. 14409.
(18) Velický, M.; Toth, P. S.; Rakowski, A. M.; Rooney, A. P.; Kozikov, A.; Woods, C. R.; Mishchenko, A.; Fumagalli, L.; Yin, J.; Zólyomi, V.; Georgiou, T.; Haigh, S. J.; Novoselov, K. S.; Dryfe, R. A. W. Exfoliation of natural van der Waals heterostructures to a single unit cell thickness. *Nat. Commun.* **2017**, *8*, No. 14410.
(19) Ray, K.; Yore, A. E.; Mou, T.; Jha, S.; Smithe, K. K. H.; Wang, B.; Pop, E.; Newaz, A. K. M. Photoresponse of natural van der Waals heterostructures. *ACS Nano* **2017**, *11*, 6024−6030.
(20) Frisenda, R.; Niu, Y.; Gant, P.; Muñoz, M.; Castellanos-Gomez, A. Naturally occurring van der Waals materials. *npj 2D Mater. Appl.* **2020**, *4*, No. 38.
(21) Frisenda, R.; Sanchez-Santolino, G.; Papadopoulos, N.; Urban, J.; Baranowski, M.; Surrente, A.; Maude, D. K.; Garcia-Hernandez, M.; van der Zant, H. S. J.; Plochocka, P.; San-Jose, P.; Castellanos-Gomez, A. Symmetry breakdown in franckeite: spontaneous strain, rippling, and interlayer moiré. *Nano Lett.* **2020**, *20*, 1141−1147.
(22) Kresse, G.; Furthmüller, J. Efficiency of ab-initio total energy calculations for metals and semiconductors using a plane-wave basis set. *Comput. Mater. Sci.* **1996**, *6*, 15−50.
(23) Perdew, J. P.; Burke, K.; Ernzerhof, M. Generalized Gradient Approximation Made Simple. *Phys. Rev. Lett.* **1996**, *77*, 3865−3868.
(24) Grimme, S.; Antony, J.; Ehrlich, S.; Krieg, H. A consistent and accurate ab initio parametrization of density functional dispersion correction (DFT-D) for the 94 elements H-Pu. *J. Chem. Phys.* **2010**, *132*, No. 154104.
(25) Togo, A.; Tanaka, I. First principles phonon calculations in materials science. *Scr. Mater.* **2015**, *108*, 1−5.
(26) Umari, P.; Pasquarello, A.; Dal Corso, A. Raman scattering intensities in α-quartz: A first-principles investigation. *Phys. Rev. B* **2001**, *63*, No. 094305.
(27) Ceriotti, M.; Pietrucci, F.; Bernasconi, M. Ab initio study of the vibrational properties of crystalline TeO_2: The alpha, beta, and gamma phases. *Phys. Rev. B* **2006**, *73*, No. 104304.
(28) Ling, X.; Liang, L.; Huang, S.; Puretzky, A. A.; Geohegan, D. B.; Sumpter, B. G.; Kong, J.; Meunier, V.; Dresselhaus, M. S. Low-frequency interlayer breathing modes in few-layer black phosphorus. *Nano Lett.* **2015**, *15*, 4080−4088.
(29) Liang, L.; Meunier, V. First-principles Raman spectra of MoS2, WS2 and their heterostructures. *Nanoscale* **2014**, *6*, 5394−5401.
(30) Gajdoš, M.; Hummer, K.; Kresse, G.; Furthmüller, J.; Bechstedt, F. Linear optical properties in the projector-augmented wave methodology. *Phys. Rev. B* **2006**, *73*, No. 045112.
(31) Liang, L.; Zhang, J.; Sumpter, B. G.; Tan, Q.-H.; Tan, P.-H.; Meunier, V. Low-frequency shear and layer-breathing modes in raman scattering of two-dimensional materials. *ACS Nano* **2017**, *11*, 11777−11802.
(32) Yuan, X.; Mayanovic, R. A. An empirical study on raman peak fitting and its application to raman quantitative research. *Appl. Spectrosc.* **2017**, *71*, 2325−2338.
(33) Calizo, I.; Balandin, A. A.; Bao, W.; Miao, F.; Lau, C. N. Temperature dependence of the raman spectra of graphene and graphene multilayers. *Nano Lett.* **2007**, *7*, 2645−2649.
(34) Huang, X.; Gao, Y.; Yang, T.; Ren, W.; Cheng, H.-M.; Lai, T. Quantitative analysis of temperature dependence of raman shift of monolayer WS2. *Sci. Rep.* **2016**, *6*, 32236.
(35) Lanzillo, N. A.; Glen Birdwell, A.; Amani, M.; Crowne, F. J.; Shah, P. B.; Najmaei, S.; Liu, Z.; Ajayan, P. M.; Lou, J.; Dubey, M.; Nayak, S. K.; O'Regan, T. P. Temperature-dependent phonon shifts in monolayer MoS_2. *Appl. Phys. Lett.* **2013**, *103*, No. 093102.
(36) Sahoo, S.; Gaur, A. P. S.; Ahmadi, M.; Guinel, M. J. F.; Katiyar, R. S. Temperature-Dependent Raman Studies and Thermal Conductivity of Few-Layer MoS2. *J. Phys. Chem. C* **2013**, *117*, 9042−9047.

https://doi.org/10.1021/acs.jpcc.1c05241
J. Phys. Chem. C 2021, 125, 21607−21613

Supporting Information:

Vibrational Properties of a Naturally Occurring Semiconducting van der Waals heterostructure

V.Z. Costa[1], Liangbo Liang[2], Sam Vaziri[3], Addison Miller[1], Eric Pop[3,4,5], and A. K. M. Newaz[1]

[1]Department of Physics and Astronomy, San Francisco State University, San Francisco, California 94132, USA

[2] Center for Nanophase Materials Sciences, Oak Ridge National Laboratory, Oak Ridge, Tennessee 37831, United States

[3]Department of Electrical Engineering, Stanford University, Stanford, California 94305, USA

[4]Department of Materials Science and Engineering, Stanford University, Stanford, California 94305, USA

[5]Precourt Institute for Energy, Stanford University, Stanford, California 94305, USA

S1: Raman spectroscopy for Pb_3SbS_4

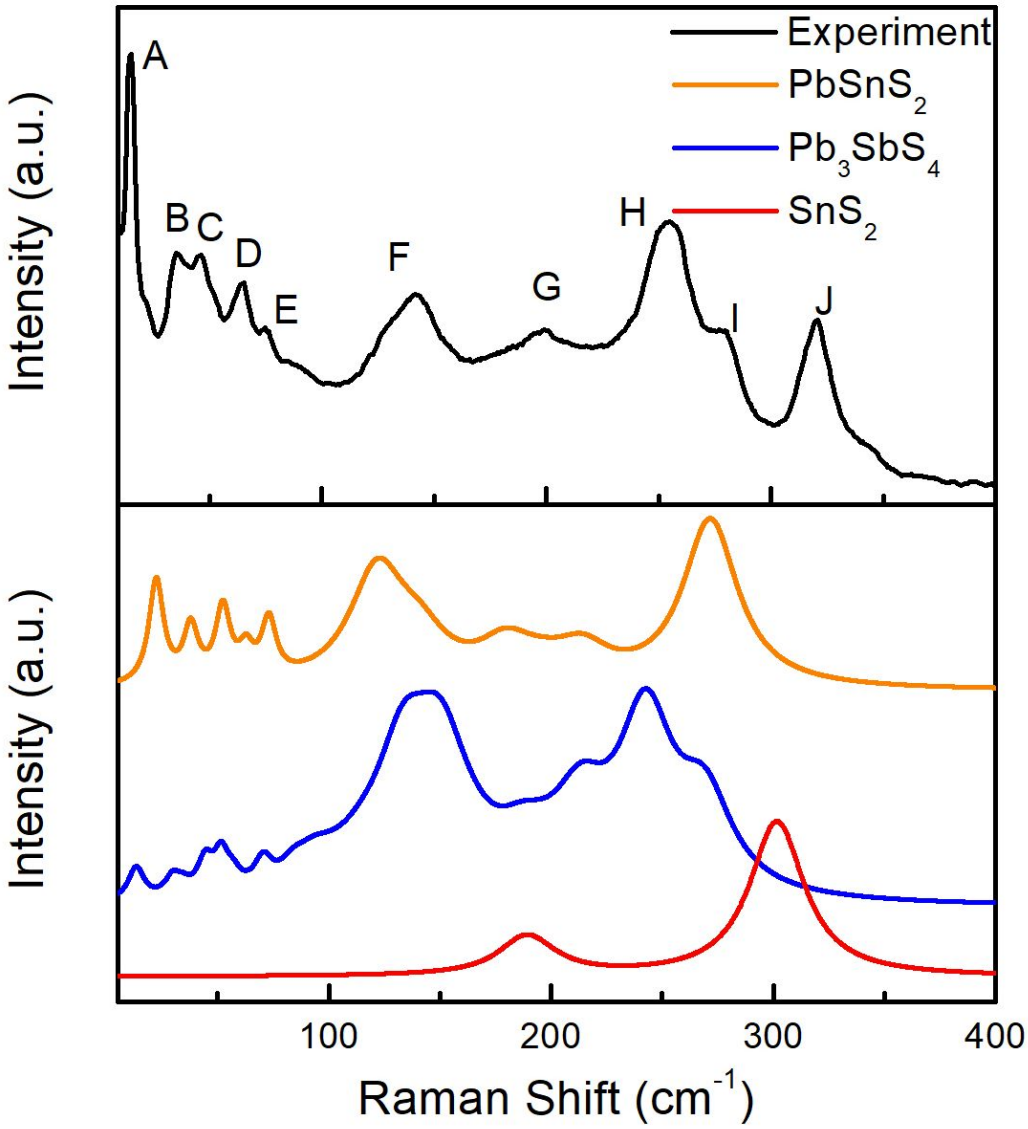

Figure S1: Raman spectroscopy of many layer Franckeite. (a) The plot presents the experimentally measured Raman spectroscopy at room temperature. The excitation laser wavelength is 633 nm. We have observed high frequency Raman modes as well as low frequency Raman modes. The Raman modes are marked alphabetically as A(14 cm^{-1}), B(35 cm^{-1}), C (45 cm^{-1}), D(64 cm^{-1}), E(75 cm^{-1}), F(140 cm^{-1}), G(195 cm^{-1}), H(256 cm^{-1}), I(276 cm^{-1}) and J(321 cm^{-1}). (b) Calculated Raman spectra of Franckeite are shown here. The upper (orange), middle (blue) and lower (red) plots present the Raman modes for $PbSnS_2$, Pb_3SbS_4 and SnS_2, respectively.

S2: Raman spectra for 532 nm and 633 nm laser excitations

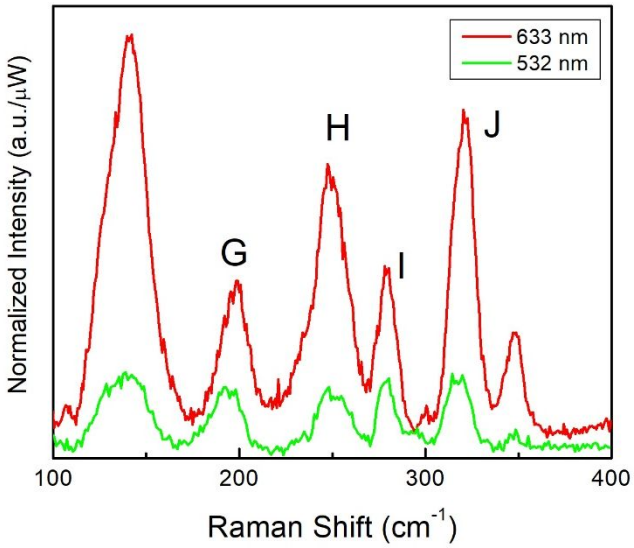

Figure S2: The Raman spectra for 532 nm laser (green line) and 633 nm laser (red line) measured at room temperature. The spectra were normalized using the measured laser power.

S3: Differential reflectivity measurements of Franckeite

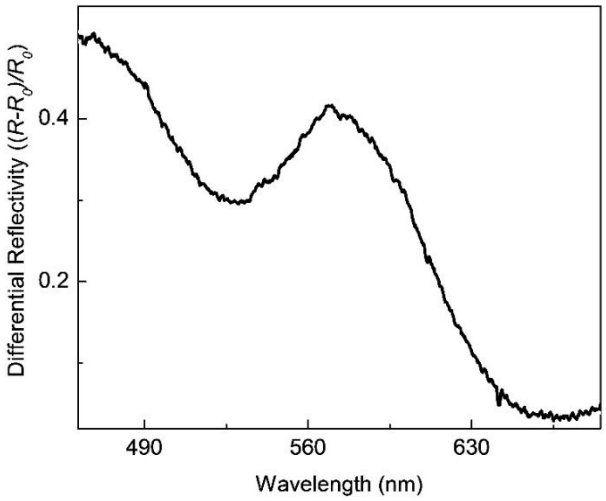

Figure S3: Differential reflectivity measurements of Franckeite. The differential reflectivity ($\frac{R-R_0}{R_0}$, where R is the change in the reflectance signal from the sample and R_0 is from off the sample location. We have used a broad band thermal light source to illuminate the sample. The reflectance signal was measured by a spectrometer with 300 lines/mm grating.

S4: Raman spectra for different thickness of Franckeite

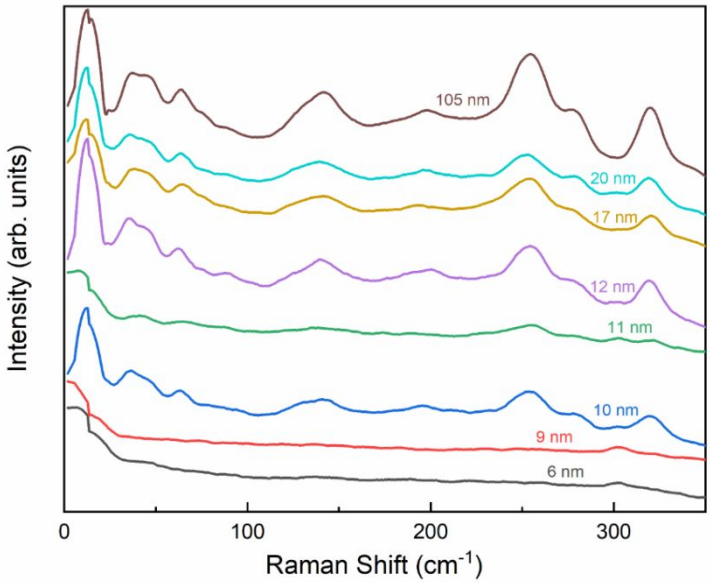

Figure S4: Raman spectra of Franckeite for different thickness. The measurements were done at room temperature and the excitation laser was 633 nm. The thickness values are shown next to the spectrums.

S5: Temperature dependent Raman Spectroscopy of Franckeite

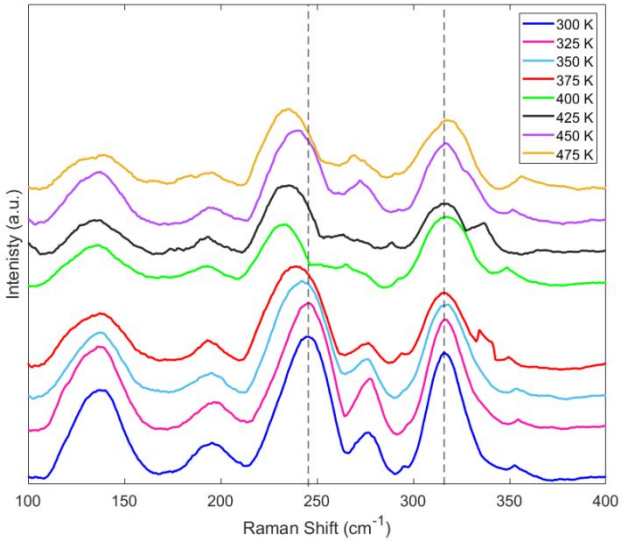

Figure S5: Raman spectra of Franckeite at different temperatures.

S6: Temperature dependent Raman Spectroscopy of Silicon

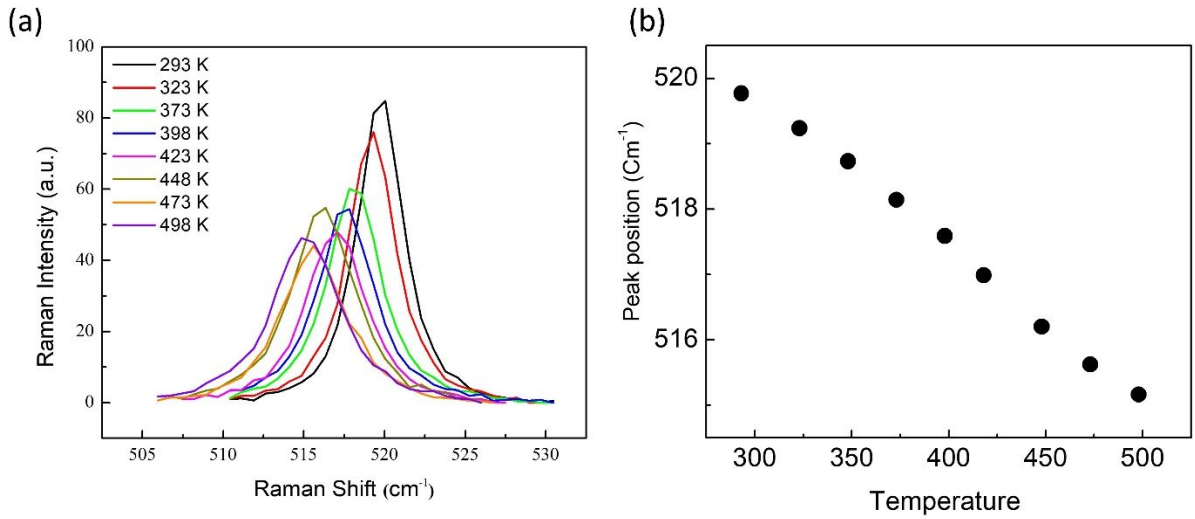

Figure S6: Temperature dependence of the vibrational mode of Si. (a) This figure presents the Raman spectra at different temperatures from 293 K to 498 K. All peaks are shifting to lower Raman shift values as we increase the temperature. (b) This plot is showing the change of the peak position with respect to the temperature.

S7: Gaussian fitting of the Raman Peak

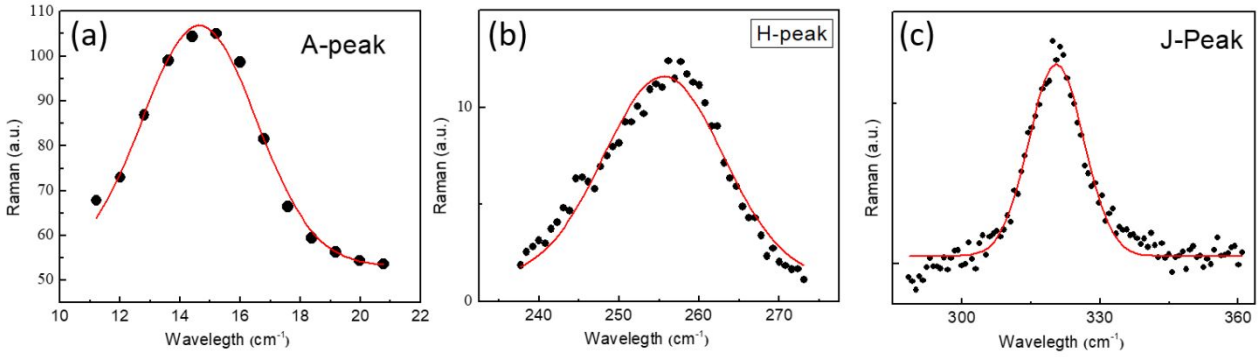

Figure S7: Gaussian fitting of the Raman peak to determine the peak position and the errors for the A peak (a) and H peak (b) and J peak (c) measured at room tempearture. The black circles and the red line represent the experimental data and the fitting line, respectively.

Table: Calculated values obtained by Gaussian fitting of the Raman peak

Peak	Peak (cm^{-1})	Error (cm^{-1})	width (cm^{-1})
A	14.64	0.06	3.80
H	255.56	0.19	14.93
J	320.51	0.14	11.92

S8: Thermal stability of the sample

We have found that the Franckeite is thermally stable. The optical image of a flake remains the same even after 18 months stored in an ambient condition.

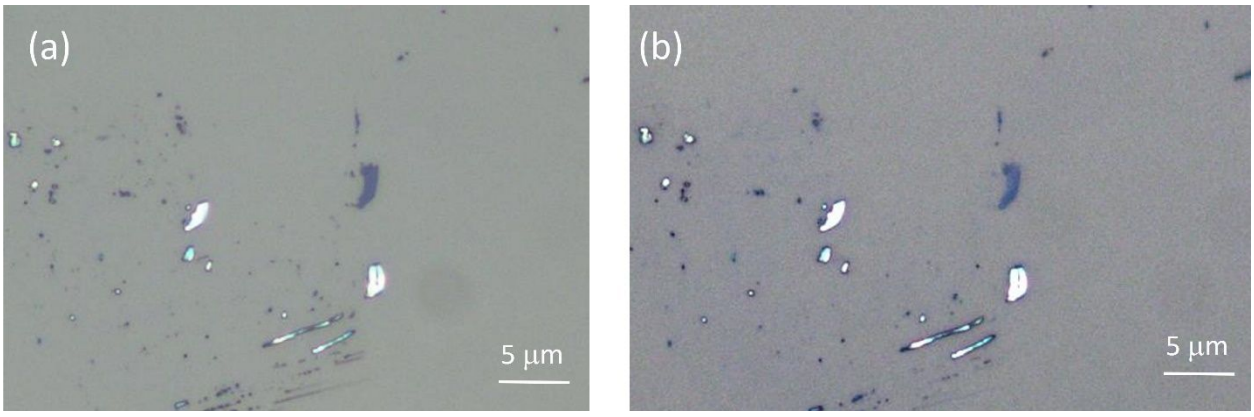

Figure S8: The optical image of a few layer Franckeite sample taken at 02/04/2020 (a) and 08/20/2021 (b).